



# Efficient atrazine degradation via photoactivated SR-AOP over S-BUC-21(Fe): The formation and contribution of different reactive oxygen species

Zi-Chen Zhang, Fu-Xue Wang, Fei Wang, Chong-Chen Wang<sup>\*</sup>, Peng Wang

Beijing Key Laboratory of Functional Materials for Building Structure and Environment Remediation, Beijing University of Civil Engineering and Architecture, Beijing 100044, PR China

Beijing Energy Conservation & Sustainable Urban and Rural Development Provincial and Ministry Co-construction Collaboration Innovation Center, Beijing University of Civil Engineering and Architecture, Beijing 100044, PR China

## ARTICLE INFO

### Keywords:

Metal-organic framework  
Atrazine  
Singlet oxygen  
Sulfate radical-advanced oxidation process  
Mechanism

## ABSTRACT

Fe-based metal organic frameworks (MOFs) as catalysts exhibited great potential in peroxymonosulfate (PMS) activation for organic pollutant decontamination. In this work, a Fe-based MOF S-BUC-21(Fe) with superior catalytic activity in PMS activation to remove atrazine (ATZ) is reported, in which ATZ was completely degraded within 20.0 min in the presence of 0.1 g/L S-BUC-21(Fe), 0.4 mM PMS and LED UV light irradiation. Both the active species capturing experiments and electron spin resonance (ESR) revealed that reactive species like  $\text{SO}_4^{\bullet-}$ ,  $\bullet\text{OH}$ ,  $\bullet\text{O}_2$ , and  $^1\text{O}_2$  could be generated continuously via  $\text{Fe}^{2+}/\text{Fe}^{3+}$  cycle along with direct or indirect photo-induced electron transfer. According to the reactive oxygen species (ROSs) contribution calculation,  $\text{SO}_4^{\bullet-}$  and  $^1\text{O}_2$  were found to play major roles in the ATZ degradation process. Furthermore, quantification and the generation pathways of  $^1\text{O}_2$  were revealed. After 5-runs experiments, S-BUC-21(Fe) exhibited outstanding stability and reusability, maintaining the morphology and structure of used S-BUC-21(Fe) along with 100.0 % ATZ degradation efficiency.

## 1. Introduction

From the 1950s, atrazine (2-chloro-4-ethylamino-9-isopropylamino-1,3,5-triazine, ATZ) was widely used as a herbicide in agriculture and forestry [1]. It was essential to remove toxic ATZ as it could be accumulated in water, soil, and even the food chain [2] to threaten human and ecological health.

Recently, advanced oxidation processes (AOPs) are proved to be efficient for decontamination by the formed reactive radicals like hydroxyl ( $\bullet\text{OH}$ ) and sulfate ( $\text{SO}_4^{\bullet-}$ ) radicals. Compared with  $\bullet\text{OH}$ , the  $\text{SO}_4^{\bullet-}$  radicals demonstrate higher redox potential, longer half-life time, and higher oxidation selectivity [3]. Thus, the sulfate radical-advanced oxidation processes (SR-AOPs) are proper for water treatment, in which  $\text{SO}_4^{\bullet-}$  is usually generated from peroxymonosulfate (PMS) or peroxodisulfate (PDS) activation [4]. PMS or PDS activation by transition metals is efficient and easy to operate, which attracts wide attention. Besides  $\text{SO}_4^{\bullet-}$ ,  $\bullet\text{OH}$  and  $\bullet\text{O}_2$  radicals, nonradical singlet oxygen ( $^1\text{O}_2$ ) was generally observed in both PMS and PDS activation systems [5], in which the  $^1\text{O}_2$  nonradical can be generated from  $\text{SO}_5^{\bullet-}$  self-reaction, PMS self-decomposition and other pathways [6]. PMS activation over

heterogeneous catalysts could be operated in the wide pH range (3.0 ~ 11.0) without massive sludge [7]. The Co-based catalysts possess excellent performance in activating PMS. However, the leached Co ions are toxic, which could lead to secondary pollution. Alternately, the Fe-based catalysts with low toxicity are preferential candidates for PS activation [8].

Due to the abundant active sites and tunable pore structures, metal-organic frameworks (MOFs) displayed versatile potential applications in catalysis [9], heavy metal reduction [10], and fluorescence sensing [11]. Some Fe-MOFs could be excited by UV and/or visible light due to rich iron-oxo clusters. Further, there are abundant coordinative unsaturated Fe sites on the surface of the Fe-MOFs. These properties can accelerate the transfer of photo-generated electron and promote ROSs generation to accomplish the degradation of organic pollutants. Many reports demonstrated that Fe-MOFs like MIL-100(Fe), MIL-101(Fe), MIL-88A(Fe) and BUC-21(Fe) exhibited good performance in photocatalysis [12–15], photo-Fenton [16], photocatalysis/photo-activated SR-AOP [17] and so on [10,18] under UV and/or visible light [19,20]. However, the research of Fe-MOFs as SR-AOPs catalysts is still in the early stage, in which the reaction mechanism and formation pathway of

<sup>\*</sup> Corresponding author.

E-mail addresses: [wangchongchen@bucea.edu.cn](mailto:wangchongchen@bucea.edu.cn), [chongchenwang@126.com](mailto:chongchenwang@126.com) (C.-C. Wang).

ROs should be further explored. In addition, 2D Fe-MOFs attract more attentions in PMS/PDS activation, since they show faster mass transfer, more exposed active sites and better water stability [21].

BUC-21(Fe), a stable 2D Fe-MOF constructed from Fe ions, *cis*-1,3-dibenzyl-2-imidazolidone-4,5-dicarboxylic acid ( $H_2L$ ) and 4,4'-bipyridine (bpy), possessed excellent photo-Fenton performance [22]. In this work, S-BUC-21(Fe) was solvothermally synthesized to be adopted as heterogeneous catalyst to activate PMS for ATZ degradation. The influence of PMS concentration, catalyst dosage, pH and inorganic anions on ATZ removal efficiency was studied in detail. Electrochemical technology was utilized to test the dynamic charge-transfer between S-BUC-21(Fe) and PMS. The  $SO_4^{\cdot-}$  and  $^1O_2$  played the primary roles in the oxidation process, which was further confirmed by the electron spin resonance (ESR) and classical ROs quenching experiments. The ROs quantifications were carried out to clarify the contributions of the corresponding ROs. Finally, the possible mechanisms of PMS activation were proposed and affirmed.

## 2. Experimental

### 2.1. Materials and characterizations

The information of the reagents, materials, characterization instruments and methods along with the data analysis were provided in the [Supplementary Information \(SI\)](#).

### 2.2. Synthesis of S-BUC-21(Fe)

The solvothermal synthesis of S-BUC-21(Fe) was carried out according to the previous report with some modifications [22]. A mixture of  $FeSO_4 \cdot 7H_2O$  (0.3 mmol), bpy (0.3 mmol) and  $H_2L$  (0.3 mmol) with 1 mL DMF and 15 mL deionized water were sealed in a 25.0 mL Teflon-lined stainless steel Parr bomb container, which was heated at 170 °C for 12 h. After cooling down gradually to room temperature, the as-prepared crystals of S-BUC-21(Fe) were collected by filtration.

### 2.3. Photoactivated SR-AOP activity of S-BUC-21(Fe)

A certain dosage of S-BUC-21(Fe) particles was added into 50.0 mL aqueous solution containing ATZ (10.0 mg/L) at room temperature in dark to reach the adsorption/desorption equilibrium. Subsequently, the PMS solution was added into ATZ solution. At the same time, the targeted solution was irradiated with 10 W LED 369 nm UV light (Beijing Perfectlight Co. Ltd., PCX-50B). During the illumination, 1.5 mL solution was filtrated at a fixed time-interval to determine the residual ATZ concentrations on liquid chromatography (LC-20A, Shimadzu, Japan).

### 2.4. Quantification of sulfate radical, superoxide radical, singlet oxygen and residual PMS

The generated sulfate radicals can react with *p*-hydroxybenzoic (HBA) to form 4-benzoquinone (BQ) [23]. The HBA and PMS with different mole ratios from 1:1 to 1:5 were mixed in 50.0 mL deionized water, and then S-BUC-21(Fe) catalyst was added. 1.5 mL aliquot was drawn out by syringe filter with 0.22  $\mu$ m PTFE membrane at set time intervals to determine the formed BQ on ultra-high performance liquid chromatography (UHPLC, Thermo Scientific Vanquish Flex). Finally, the  $SO_4^{\cdot-}$  concentration could be determined based on the stoichiometric ratio of sulfate radical and BQ.

Nitroblue terazolium (NBT) ( $5.0 \times 10^{-5}$  mol/L,  $\lambda = 259$  nm) was used as a probe to quantify superoxide radical ( $\bullet O_2^-$ ). The concentration of NBT was detected by UV-vis spectrophotometer to quantitatively analyze the generation of  $\bullet O_2^-$ . The process was similar to that of ATZ degradation, except that the ATZ was replaced by NBT [24].

The 1,3-diphenylisobenzofuran (DPBF) (0.2 mol/L,  $\lambda = 410$  nm) was used as a trapping agent to quantify singlet oxygen ( $^1O_2$ ). The

concentration of  $^1O_2$  was obtained by the consumed DPBF due to their stoichiometric ratio was 1:1. The process was similar to that of ATZ degradation, except that the ATZ was replaced by DPBF [25].

The residual PMS was detected by mixing 0.5 mL reaction solution and 4.5 mL KI solution (1.11 g/L) under stirring for 30.0 min to ensure complete reaction between  $I^-$  and  $HSO_5^-$  (Eqs. S1 and S2). The concentration of the formed  $I_3$ , proportional to PMS, was determined by UV-visible spectrophotometer at  $\lambda_{max} = 352$  nm [26].

## 3. Results and discussion

### 3.1. Characterizations of S-BUC-21(Fe)

The scanning electronic microscopy (SEM) images, as shown in [Fig. 1a](#), demonstrated that the S-BUC-21(Fe) crystals showed a micron-sized square sheet with a size of ca.  $50 \mu m \times 50 \mu m \times 5 \mu m$ . According to the CIF file (CCDC 2100429) [22], in the crystal structure of S-BUC-21(Fe), the two types of Fe atoms (Fe1 and Fe2) with different coordination modes are bridged by completely protonated  $L^{2-}$  anions and neutral bpy ligands into 2D network. The powder XRD patterns of the as-prepared S-BUC-21(Fe), as depicted in [Fig. 1b](#), matched well with the previous report and the simulated one from the single crystal structure data of above-mentioned CIF file (CCDC 2100429) [22]. As shown in [Fig. 1c](#), The Fourier-transform infrared (FTIR) spectrums displayed the characteristic peaks like Fe-O stretching vibration ( $482 \text{ cm}^{-1}$ ), benzene ring of ligand ( $702 \text{ cm}^{-1}$ ) and asymmetric and symmetric vibration of the carboxyl group ( $1603$  and  $1451 \text{ cm}^{-1}$ ) of the as-obtained S-BUC-21(Fe).

It was demonstrated from UV-vis DRS that S-BUC-21(Fe) could absorb a wide range of wavelength from 300 nm to 600 nm ([Fig. 1d](#)). And the band gap was calculated as  $E_g = 1.30$  eV [27], based on UV-vis DRS data (inset of [Fig. 1d](#)), which is closed to the reported one [22]. According to Mott-Schottky (MS) plot illustrated in [Fig. 1e](#), S-BUC-21(Fe) is *n*-type catalyst [28] and the tangent of MS curves on the x-axis is  $-0.63$  eV (vs. Ag/AgCl, pH = 7.0). According to Eqs. S3 and S4 [29], the  $E_{LUMO}$  and  $E_{HOMO}$  were determined to be ca.  $-0.414$  eV and  $0.886$  eV, respectively.

### 3.2. Photoactivated SR-AOP performances of S-BUC-21(Fe)

#### 3.2.1. ATZ degradation

The ATZ was used as pollutant model to evaluate the photoactivated SR-AOP degradation performance of S-BUC-21(Fe) under UV light. Control experiments in different light source conditions were conducted ([Fig. 2a](#)). It was observed that only 15 % ATZ was adsorbed onto S-BUC-21(Fe) within 20.0 min, which may be attributed to weak interactions like van der Waals and hydrogen bonding interactions [30,31]. Herein, under dark condition, the S-BUC-21(Fe) showed weak adsorption activity toward ATZ. In addition, 22.92 % and 11.24 % ATZ were removed in "PMS + 369 nm LED UV light" system and "S-BUC-21(Fe) + 369 nm LED UV light" system, respectively. More than 96.81 % of ATZ was decomposed within 20.0 min in presence of 0.4 mM PMS and 0.3 g/L S-BUC-21(Fe) under UV light (369 nm) irradiation, which was higher than those under various visible light irradiations (32.20 % for 630 nm, 37.39 % for 595 nm, 37.95 % for 520 nm, 50.97 % for 485 nm, 61.16 % for 450 nm, 70.98 % for 420 nm), as shown in [Fig. S1](#). From these points, the high ATZ removal efficiency could be attributed to that PMS was activated by S-BUC-21(Fe) and UV light irradiation.

The SR-AOP activity is usually influenced by PMS concentration because it is the main source of ROs generation. As depicted in [Fig. S2a](#), the ATZ degradation efficiencies increased from 53.08 % to 100.0 % in 20.0 min with the PMS concentrations increasing from 0.2 to 0.4 mM. However, the ATZ removal efficiencies decreased from 100.0 % to 93.71 % with further increasing PMS addition up to 0.5 mM, which might attribute to the scavenging of excessive  $SO_4^{\cdot-}$  (Eqs. S5 and S6).

As depicted in [Fig. 2b](#), ca. 90.0 % ATZ degradation efficiencies were accomplished within 20.0 min in the pH range from 3.5 to 9.5,

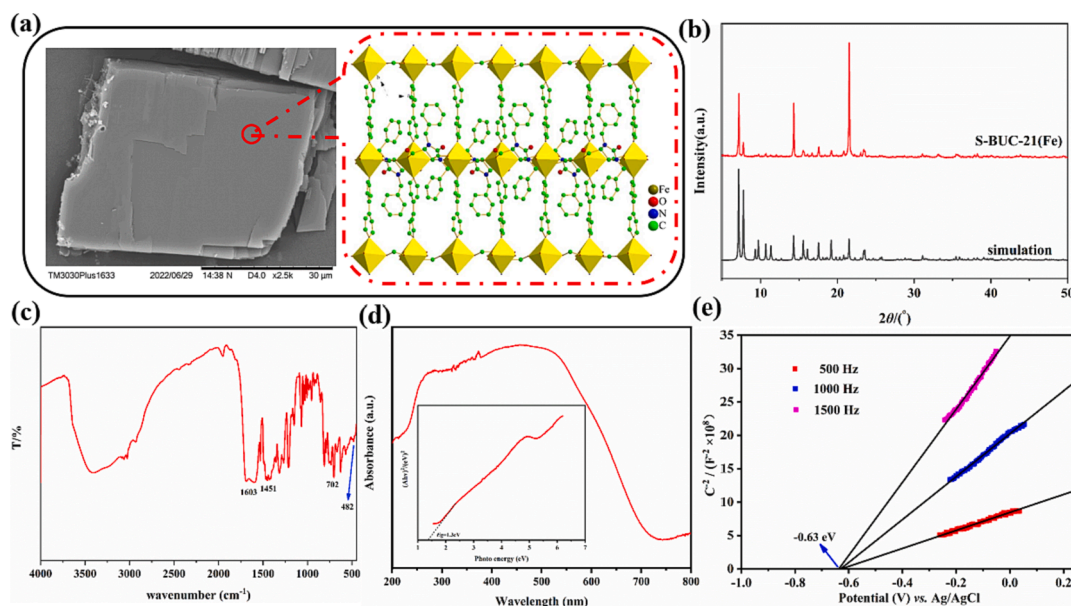


**Fig. 1.** (a) SEM image and crystal structure; (b) XRD pattern; (c) FTIR spectra; (d) The UV-Vis DRS and band energy ( $E_g$ ) plots (inset) and (e) Mott-Schottky curves of S-BUC-21(Fe).

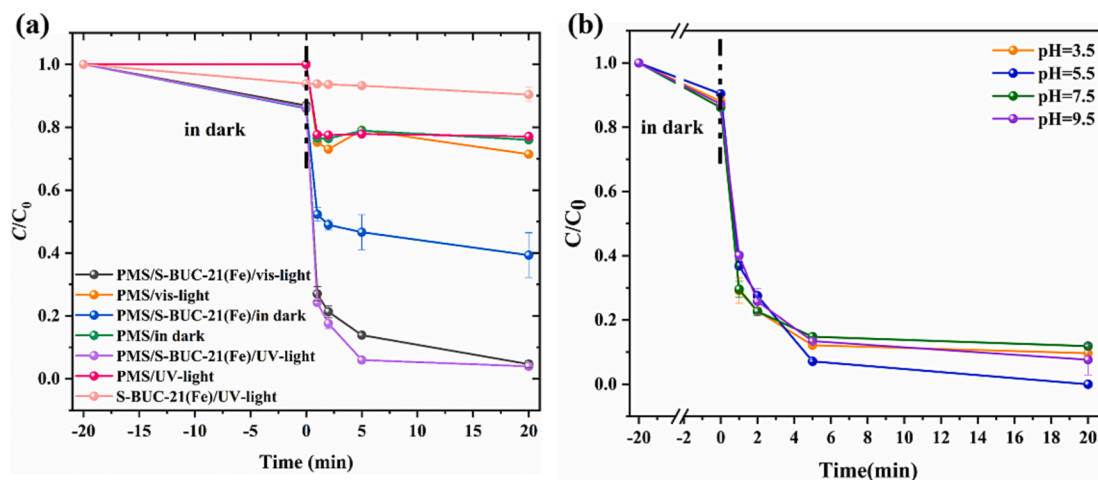


**Fig. 2.** (a) The ATZ degradation efficiencies under different conditions; (b) The influence of initial pH. Reaction conditions: (a) ATZ = 10.0 mg/L; pH = 5.56; S-BUC-21(Fe) = 0.3 g/L; PMS = 0.4 mM; volume = 50.0 mL; (b) The initial pH was changed, and the other factors were fixed.

indicating wide pH suitability of S-BUC-21(Fe). Under acidic conditions (pH = 3.5), both homogeneous and heterogeneous reaction may contribute to ATZ degradation, since ca. 3.0 mg/L Fe ion was leached from S-BUC-21(Fe). While under neutral and alkaline conditions (pH = 5.5–9.5), the leaching Fe ion was only 0.3 mg/L, indicating that heterogeneous reaction dominated the reaction.

In Fig. S2b, the ATZ degradation kinetics also increased with increasing S-BUC-21(Fe) dosage from 0.0 g/L to 0.3 g/L ( $k_{0.0}$  g/L = 0.0003 min⁻¹,  $k_{0.1}$  g/L = 0.4300 min⁻¹,  $k_{0.3}$  g/L = 0.5223 min⁻¹). Although ATZ could be removed completely with addition of 0.3 g/L S-BUC-21(Fe), the agglomeration, under 0.3 g/L catalysts condition, would influence the full utilization of exposed active sites and the UV light. Additionally, S-BUC-21(Fe) showed good photoactivated SR-AOP performance for both high (20.0 mg/L) and low (5.0 mg/L) ATZ concentrations (Fig. S2c).

### 3.2.2. Influences of co-existing inorganic anions

The influences of different inorganic anions including Cl⁻, NO₃⁻, HCO₃⁻, SO₄²⁻ and H₂PO₄⁻ on ATZ degradation were investigated and the

corresponding concentrations referred the surface water quality of Beijing [32]. As shown in Fig. S2d, the negative effects on ATZ degradation in the presence of Cl⁻ and NO₃⁻ ( $k_{obs}$  decreased from 0.4300 min⁻¹ to 0.1470 and 0.2233 min⁻¹) might be due to the generation of some ROSSs like Cl• ( $E^0 = 2.59$  V) [33], Cl₂•⁻ ( $E^0 = 2.30$  V) [34,35] and NO₃• ( $E^0 = 2.3–2.5$  V) [36,37] (Eqs. R1–R6 in Table S3) with lower redox potentials than those of SO₄•⁻ and •OH. Besides, the H₂PO₄⁻, acting as masking agent, might reduce the active metal sites on the Fe-based catalyst surface [22]. Therefore, H₂PO₄⁻ exerted a negative impact on the degradation process of ATZ. The SO₄²⁻ and HCO₃⁻ preferred to quench ROSSs to inhibit the degradation process (Eqs. R7–R9 in Table S3) [38–40]. The SO₄•⁻ could interact with H₂O and OH⁻ to produce H⁺, leading to that the pH decreased from ca. 5.5 to 3.5 (Fig. S2e). The initial pH increased from 5.56 to 8.22 after HCO₃⁻ addition. Fortunately, 90 % ATZ could be still removed under pH = 9.5 (Fig. 2b). Therefore, the negative effect of HCO₃⁻ on ATZ degradation might result from the consumption of ROSSs rather than the change of the pH.



### 3.3. Possible mechanism of the photoactivated SR-AOP over S-BUC-21 (Fe)

#### 3.3.1. Electrochemical tests of S-BUC-21(Fe)

The electrochemical impedance spectroscopy (EIS) of S-BUC-21(Fe) was carried out to verify the charge-transfer resistance. As presented in Fig. 3a, S-BUC-21(Fe) system showed the minimum semicircular under the UV + S-BUC-21(Fe) + PMS condition, meaning better charge transfer over S-BUC-21(Fe).

#### 3.3.2. The role of Fe active sites

Our group previously adopted phosphate to mask Fe sites of BUC-21 (Fe) [22], in which the chloroquine phosphate (CQ) removal efficiencies decreased from 100.0 % to 68.3 %. In this work, both phosphate masking and PMS quantification experiments were conducted to further verify the synergism between PMS and the exposed Fe sites under UV light. As shown in Fig. 3b, the degradation efficiencies of ATZ decreased from 100.0 % to 33.5 % with addition of 0.2 mM phosphate in reaction system. The consumption of PMS also decreased from 100.0 % to 20.0 %. The results not only suggested the important role of exposed Fe (both  $\text{Fe}^{2+}$  and  $\text{Fe}^{3+}$ ) sites, but also confirmed the interaction between S-BUC-21(Fe) and PMS in UV/S-BUC-21(Fe)/PMS system.

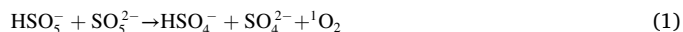
#### 3.3.3. The identification of the reactive species

It is usually considered that the various radicals like  $\text{SO}_4^{\bullet-}$ ,  $\bullet\text{OH}$  and  $\bullet\text{O}_2^-$ , as well as the nonradical  $^1\text{O}_2$  play the main role in organic pollutants degradation via PMS activation [41]. Theoretically, the above-mentioned ROSS could be generated in SR-AOP process to promote the degradation of ATZ. Because the reduction potentials of these species ( $\text{SO}_4^{\bullet-}$ :  $E^0 = 2.5\text{--}3.1\text{ V}$ ,  $\bullet\text{OH}$ :  $E^0 = 1.8\text{--}2.7\text{ V}$ ,  $\bullet\text{O}_2^-$ :  $E^0 = -0.33\text{ V}$ , and  $^1\text{O}_2$ :  $E^0 = 0.65\text{ V}$  vs NHE) are more positive than LUMO position ( $-0.414\text{ eV}$ ) of S-BUC-21(Fe) [42,43], the photo-excited electrons could activate PMS to form these ROSS.

The electron spin resonance (ESR) technology was used to detect the ROSSs generated in the UV/S-BUC-21(Fe)/PMS system. As shown in

Fig. 3c-e, the characteristic signals of  $\text{DMPO} \cdot \text{SO}_4^{\bullet-}/\bullet\text{OH}$  (1:2:2:1) and  $\text{DMPO} \cdot \bullet\text{O}_2^-$  (1:1:1:1) were recorded during the reaction. Similarly, the typical three-line spectrum of  $\text{TEMP} \cdot ^1\text{O}_2$  was also clearly detected. The results indicated that  $\text{SO}_4^{\bullet-}$ ,  $\bullet\text{OH}$ ,  $\bullet\text{O}_2^-$  and  $^1\text{O}_2$  were generated in UV/S-BUC-21(Fe)/PMS system.

Generally, the specific signals of  $\text{DMPO} \cdot \text{SO}_4^{\bullet-}/\bullet\text{OH}/\bullet\text{O}_2^-$  were hardly detected, while the weak signal of  $\text{TEMP} \cdot ^1\text{O}_2$  could be observed, when PMS was present in the system alone [44,45]. Thus,  $\bullet\text{OH}$  and  $\text{SO}_4^{\bullet-}$  could hardly be formed by PMS self-decomposition (Eq. (1)) [46]. The intensities of the detected ROSSs peaks markedly increased under UV light irradiation, indicating that UV light may facilitate the generation of ROSSs to improve the corresponding SR-AOP performance. Considering that the signals of  $\text{SO}_4^{\bullet-}$ ,  $\bullet\text{OH}$ ,  $\bullet\text{O}_2^-$  and  $^1\text{O}_2$  were presented in the ESR on a qualitative level, the classical quenching experiments were also used to further confirm the role of above-mentioned ROSSs.



The tertiary butyl alcohol (TBA) and methanol (MeOH) were used as selective radical scavengers for  $\bullet\text{OH}$  and  $\text{SO}_4^{\bullet-}$  due to that TBA can prefer to react with  $\bullet\text{OH}$  and MeOH reacts quickly with  $\text{SO}_4^{\bullet-}$  [20,47,48]. Also, L-Ascorbic acid (LAA) and L-Histidine (L-His.) as scavengers are utilized to quench  $\bullet\text{O}_2^-$  ( $3.4 \times 10^9 \text{ M}^{-1} \text{ s}^{-1}$ ) and  $^1\text{O}_2$  ( $3.2 \times 10^7 \text{ M}^{-1} \text{ s}^{-1}$ ) [49]. As depicted in the Fig. 4a, with the addition of different scavengers, the first-order rate constants can be sorted as:  $k_{\text{L-His.}} (0.0218 \text{ min}^{-1}) < k_{\text{MeOH}} (0.1906 \text{ min}^{-1}) < k_{\text{LAA}} (0.2330 \text{ min}^{-1}) < k_{\text{TBA}} (0.4274 \text{ min}^{-1}) < k_{\text{blank}} (0.430 \text{ min}^{-1})$ . L-His. displayed significant inhibition towards ATZ degradation (ca. 90.0 %), followed by methanol (ca. 30.0 %). Additionally, ATZ removal efficiencies decreased to 77.29 % and 95.98 % after the introduction of LAA and TBA, respectively. In short, the inhibition effects of different scavengers were arranged as L-His. > MeOH > L-Ascorbic acid > TBA. These observations indicated that both  $\text{SO}_4^{\bullet-}$  and  $^1\text{O}_2$  played important roles in ATZ degradation in UV/S-BUC-21(Fe)/PMS system. As further adding the scavengers, the degradation of ATZ was inhibited significantly.

To further identify the main radicals in ATZ destruction, the relative

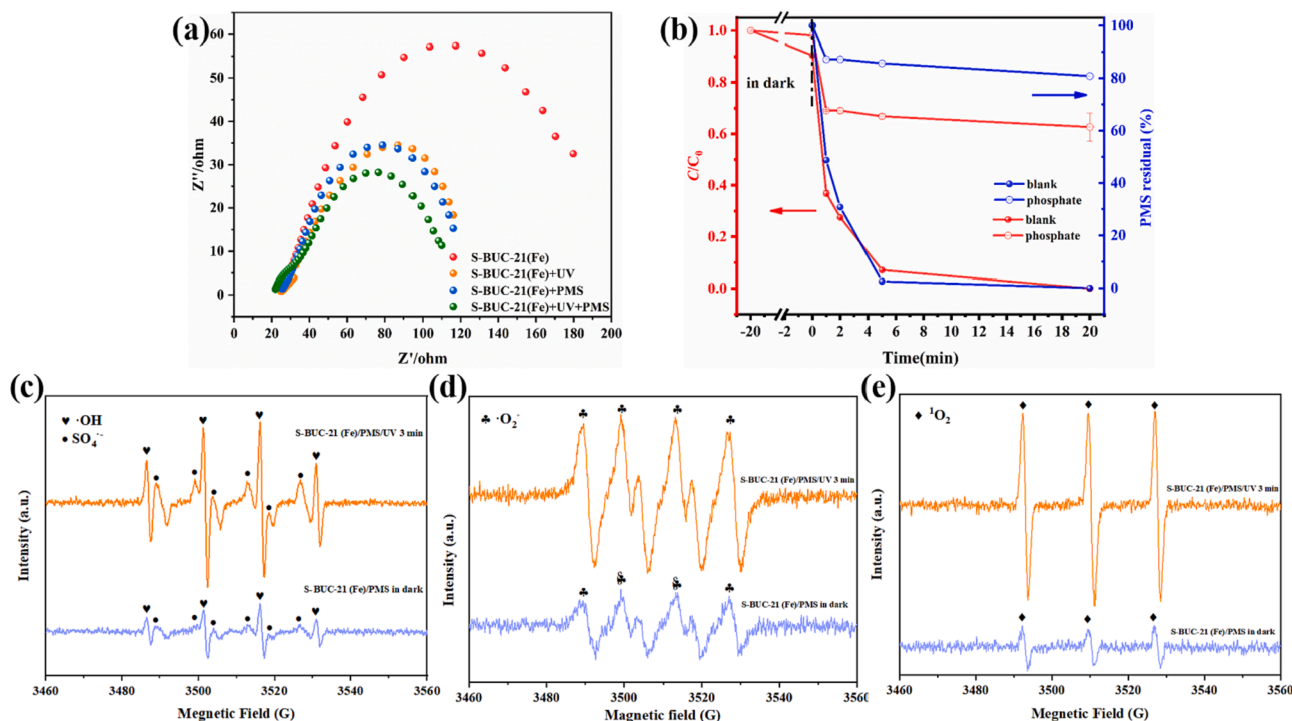


**Fig. 3.** (a) Electrochemical impedance spectroscopy analysis; (b) The ATZ degradation efficiencies and residual PMS before and after the addition of phosphate. Reaction conditions: ATZ = 10.0 mg/L; pH = 5.56; S-BUC-21(Fe) = 0.1 g/L; PMS = 0.4 mM; volume = 50.0 mL; phosphate = 0.2 mM. ESR spectra of (c)  $\text{DMPO} \cdot \text{SO}_4^{\bullet-}/\bullet\text{OH}$ ; (d)  $\text{DMPO} \cdot \bullet\text{O}_2^-$  and (e)  $\text{TEMP} \cdot ^1\text{O}_2$ . Reaction conditions:  $\text{DMPO} = \text{TEMP} = 100\text{ mM}$ .



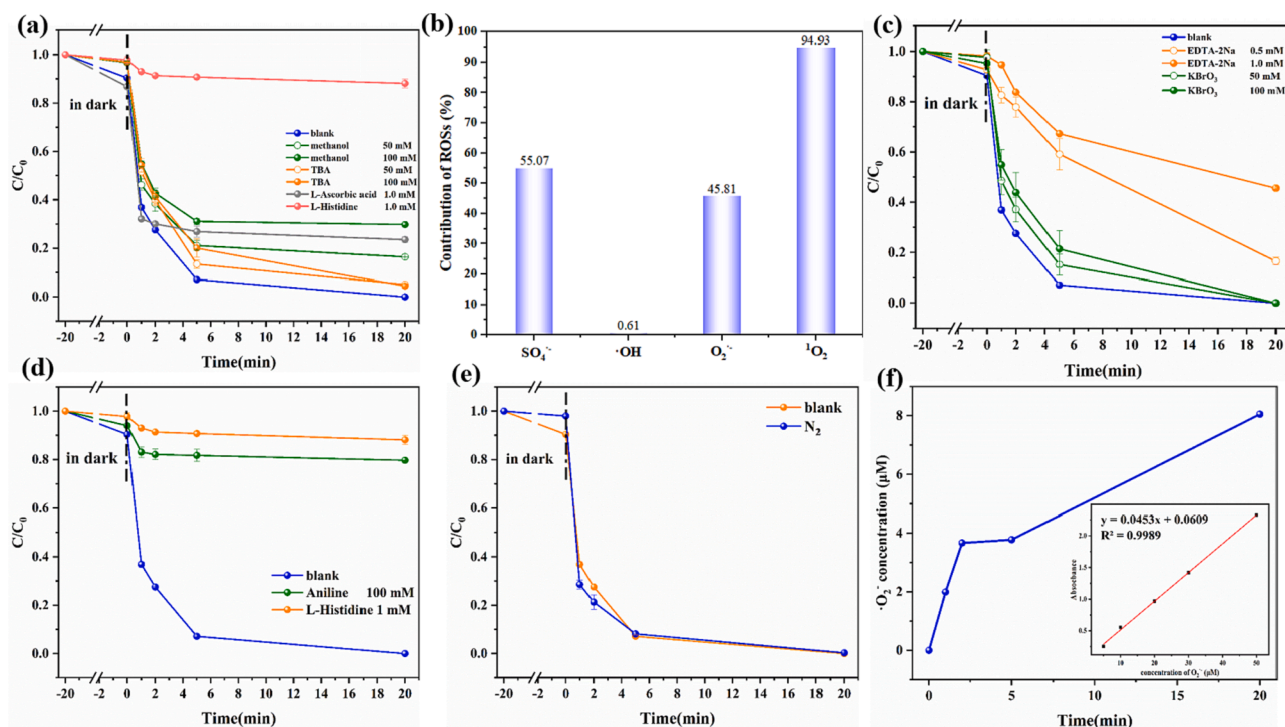


**Fig. 4.** (a) Quenching experiments with different scavengers for ATZ degradation; (b) The contribution of ROSs; (c) The capturing experiment of e<sup>-</sup> and h<sup>+</sup>; (d) The capturing experiment of SO<sub>4</sub><sup>•-</sup>; (e) The role of dissolved oxygen; (f) The concentration of the formed •O<sub>2</sub>. Reaction conditions: ATZ = 10.0 mg/L; pH = 5.56; S-BUC-21 (Fe) = 0.1 g/L; PMS = 0.4 mM; volume = 50.0 mL.

contributions of above-mentioned ROSs were calculated. It was affirmed that the rate constant (*k*) of the pseudo-first kinetics could be adopted to calculate the ROSs contribution ratios in the *p*-arsanilic acid degradation via the PMS activation over CuFe<sub>2</sub>O<sub>4</sub> [50]. It was feasible to calculate ROSs contributions following the above-described method [50,51] considering that the ATZ degradation process in the S-BUC-21 (Fe)/PMS/UV system fitted well with the pseudo-first kinetics system. The contribution ratios of •OH, •O<sub>2</sub><sup>•-</sup> and <sup>1</sup>O<sub>2</sub> were calculated according to Eq. (2). And, SO<sub>4</sub><sup>•-</sup> contribution ratio was calculated by Eq. (3) [50,52]. As seen in Fig. 4b, the relative contribution ratios of SO<sub>4</sub><sup>•-</sup>, •OH, •O<sub>2</sub><sup>•-</sup> and <sup>1</sup>O<sub>2</sub> were identified as 55.07 %, 0.60 %, 45.81 % and 94.93 %, respectively. Combined with the quenching experiments verdicts and the calculation of the ROSs contribution, the main roles of SO<sub>4</sub><sup>•-</sup> and <sup>1</sup>O<sub>2</sub> in ATZ degradation were preliminarily confirmed.

$$\text{Relative contribution of ROSs} = \frac{k_{\text{obs}} - k_{\text{obs}}(\text{quencher})}{k_{\text{obs}}} \times 100\% \quad (2)$$

$$\text{Relative contribution of sulfate radical} = \frac{k_{\text{TBA}} - k_{\text{MeOH}}}{k_{\text{obs}}} \times 100\% \quad (3)$$

### 3.3.4. Singlet oxygen generation in UV/S-BUC-21(Fe)/PMS system

Considering the most inhibition quenching experiment and the highest contribution ratio (94.93 %), the mechanisms of <sup>1</sup>O<sub>2</sub> formation in UV/S-BUC-21(Fe)/PMS system need to be further investigated. Three possible pathways were proposed to clarify the <sup>1</sup>O<sub>2</sub> formation in UV/S-BUC-21(Fe)/PMS system (Table 1). In pathway I, the electrons were transported from PMS to Fe<sup>3+</sup> of S-BUC-21(Fe), which could empower PMS oxidation to form SO<sub>5</sub><sup>•-</sup> radicals for reacting with water molecules to produce <sup>1</sup>O<sub>2</sub> (R1 – R5) [6,53]. Pathway II depended on indirect conversion of •O<sub>2</sub><sup>•-</sup> (R6 – R13) [53,54]. In pathway III, the PMS followed the self-decomposition process to generate <sup>1</sup>O<sub>2</sub> (R14) [6].

Based on above-mentioned pathways, S-BUC-21(Fe) could be excited to yield the photo-generated electrons (e<sup>-</sup>) and holes (h<sup>+</sup>) under UV light irradiation. Potassium bromate (KBrO<sub>3</sub>) and EDTA-2Na were as scavengers for e<sup>-</sup> and h<sup>+</sup> [61]. As shown in Fig. 4c, the addition of KBrO<sub>3</sub>

**Table 1**

Reactions related to <sup>1</sup>O<sub>2</sub> formation in UV/S-BUC-21(Fe)/PMS system.

Pathways	Reactions	References
Pathway I	R1: HSO <sub>5</sub> <sup>-</sup> → SO <sub>5</sub> <sup>•-</sup> + H <sup>+</sup> + e <sup>-</sup>	[55]
	R2: Fe <sup>3+</sup> + e <sup>-</sup> → Fe <sup>2+</sup>	This study
	R3: 2 SO <sub>5</sub> <sup>•-</sup> + H <sub>2</sub> O → 2HSO <sub>4</sub> <sup>-</sup> + 1.5 <sup>1</sup> O <sub>2</sub>	[56]
	R4: SO <sub>5</sub> <sup>•-</sup> + SO <sub>5</sub> <sup>•-</sup> → S <sub>2</sub> O <sub>8</sub> <sup>2-</sup> + <sup>1</sup> O <sub>2</sub>	[55]
	R5: SO <sub>5</sub> <sup>•-</sup> + SO <sub>5</sub> <sup>•-</sup> → 2SO <sub>4</sub> <sup>2-</sup> + <sup>1</sup> O <sub>2</sub>	[55]
Pathway II	R6: UV + S-BUC-21(Fe) → e <sup>-</sup> + h <sup>+</sup>	This study
	R7: O <sub>2</sub> + e <sup>-</sup> → •O <sub>2</sub> <sup>•-</sup>	[57]
	R8: •O <sub>2</sub> <sup>•-</sup> + h <sup>+</sup> → <sup>1</sup> O <sub>2</sub>	[57]
	R9: HSO <sub>5</sub> <sup>-</sup> → SO <sub>5</sub> <sup>•-</sup> + H <sup>+</sup>	[58]
	R10: SO <sub>5</sub> <sup>•-</sup> + H <sub>2</sub> O → SO <sub>4</sub> <sup>2-</sup> + H <sub>2</sub> O <sub>2</sub>	[59]
	R11: H <sub>2</sub> O <sub>2</sub> + •OH → •HO <sub>2</sub> <sup>•</sup> + H <sub>2</sub> O	[54]
	R12: •HO <sub>2</sub> <sup>•</sup> → H <sup>+</sup> + •O <sub>2</sub> <sup>•-</sup>	[54]
	R13: 2•O <sub>2</sub> <sup>•-</sup> + 2H <sub>2</sub> O → H <sub>2</sub> O <sub>2</sub> + 2OH <sup>-</sup> + <sup>1</sup> O <sub>2</sub>	[54]
Pathway III	R14: HSO <sub>5</sub> <sup>-</sup> + SO <sub>5</sub> <sup>•-</sup> → SO <sub>4</sub> <sup>2-</sup> + HSO <sub>4</sub> <sup>-</sup> + <sup>1</sup> O <sub>2</sub>	[60]

exerted little influence on ATZ degradation. Conversely, the ATZ degradation efficiencies decreased largely to 54.75 % with addition of EDTA-2Na (*k*<sub>obs</sub> = 0.037 min<sup>-1</sup>). It was deemed that h<sup>+</sup> was also responsible for ATZ degradation in the UV/S-BUC-21(Fe)/PMS system.

Aniline was adopted as scavenger for SO<sub>5</sub><sup>•-</sup> (*k*<sub>AN</sub>, SO<sub>5</sub><sup>•-</sup> = (3 – 5.8) × 10<sup>6</sup> M<sup>-1</sup> s<sup>-1</sup>, SO<sub>5</sub><sup>•-</sup>: E<sup>0</sup> = 1.1 V) [62,63] to verify whether pathway I was the main transformation routine of <sup>1</sup>O<sub>2</sub>. As depicted in Fig. 4d, the addition of 100.0 mM aniline could greatly inhibit the ATZ degradation (23.40 %). Theoretically, SO<sub>5</sub><sup>•-</sup> can generate <sup>1</sup>O<sub>2</sub> via rapid self-reaction because of the high reaction rate (~2 × 10<sup>8</sup> M<sup>-1</sup> s<sup>-1</sup>) and low activation energy (7.4 ± 2.4 kcal mol<sup>-1</sup>) [55], indicating that SO<sub>5</sub><sup>•-</sup> is probably the main source of <sup>1</sup>O<sub>2</sub> generation. But the degree of inhibition was less than that of L-His., suggesting that <sup>1</sup>O<sub>2</sub> might also be generated from

other pathways.

As shown in pathway II,  $^1\text{O}_2$  could be yielded from the indirect conversion of  $\bullet\text{O}_2^-$ . Combining with above analyses of both ESR and scavenger experiments, it could be concluded that  $\bullet\text{O}_2^-$  was involved in the system. There might be two possible paths to form  $\bullet\text{O}_2^-$ : (i) the dissolved oxygen (DO) captured  $e^-$  to generate  $\bullet\text{O}_2^-$  (R5-R7) and (ii) the generation of  $\text{H}_2\text{O}_2$  from reaction of  $\text{HSO}_5^-$  with  $\text{H}_2\text{O}$  contributed to the  $\bullet\text{O}_2^-$  production. And these two paths have been verified, respectively. The nitrogen gas was injected to the ATZ solution for 30.0 min and kept during the whole reaction to eliminate DO. As depicted in Fig. 4e, the unsuppressed degradation of ATZ in the  $\text{N}_2$ -saturated UV/S-BUC-21(Fe)/PMS system revealed that the conversion of  $\text{SO}_5^{\bullet-}$  directly contributed to the formation of  $^1\text{O}_2$  rather than DO. And the result has been further verified by quantification  $\bullet\text{O}_2^-$  experiment. As depicted in Fig. 4f, the concentration of  $\bullet\text{O}_2^-$  was nearly 8  $\mu\text{M}$ , implying that the indirect conversion of  $\bullet\text{O}_2^-$  could be a possible way to generate  $^1\text{O}_2$  [24]. In the pathway III, the generation of  $^1\text{O}_2$  from PMS self-decomposition was negligible [56].

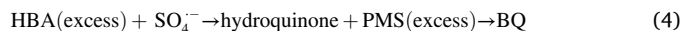
To clearly validate the role of  $^1\text{O}_2$  in UV/S-BUC-21(Fe)/PMS system, quantitative experiment of  $^1\text{O}_2$  was carried out. In Fig. S3, the concentration of  $^1\text{O}_2$  was achieved 0.2 mM in the first minute. Also, the generation of ROSs was a gradual accumulation process, therefore, the concentration of  $^1\text{O}_2$  should be greater than 0.2 mM in UV/S-BUC-21(Fe)/PMS system.

### 3.3.5. The role of sulfate radical in UV/S-BUC-21(Fe)/PMS system

According to ROSs contribution calculation (3.3.3), it was worth to noting that the sum of contributions of these radicals was far more than 100 %. It was probably attributed to that MeOH and TBA can simultaneously consume the surface-bound radicals [64]. Potassium iodide (KI) was used to quench surface-bound  $\text{SO}_4^{\bullet-}$  and  $\bullet\text{OH}$  [65]. As depicted in Fig. 5a, in the presence of KI, the  $k_{\text{obs}}$  descended sharply to 0.0007  $\text{min}^{-1}$ , suggesting that the synergistic influence of surface-bound  $\text{SO}_4^{\bullet-}$  and  $\bullet\text{OH}$  made a certain contribution to the degradation. According to the modeling results of Lin and Gurol [66], the half-life time of  $\text{SO}_4^{\bullet-}$  was longer than  $\bullet\text{OH}$ . Therefore, the  $\bullet\text{OH}$  radicals preferred to interact with the adjacent targeted pollutants rather than the far-away ones [67]. These results were consistent with the dominant role of  $\text{SO}_4^{\bullet-}$  in ATZ decomposition in the UV/S-BUC-21(Fe)/PMS.

The combination of qualitative and quantitative analysis could be more convincing. Hence, quantification of  $\text{SO}_4^{\bullet-}$  was tested.  $\text{SO}_4^{\bullet-}$  can react with HBA to generate BQ (Eq. (4)) [68], in which the amount of BQ is proportional to the  $\text{SO}_4^{\bullet-}$  concentration. As shown in Fig. 5b, the  $\text{SO}_4^{\bullet-}$  concentration increased up to 24.06  $\mu\text{M}$  gradually along with an upward trend. Theoretically, the  $\text{SO}_4^{\bullet-}$  radicals should be accumulated gradually as the reaction proceeded. However, the  $\text{SO}_4^{\bullet-}$  concentrations decreased from 24.06 to 15.85  $\mu\text{M}$  after 5.0 min. To explain this observation, the residual PMS was tested, in which PMS was almost consumed completely (up to 97.48 %) in 5.0 min (Fig. 5c). In addition, partial intermediate products might consume the residual PMS to result in the

declining  $\text{SO}_4^{\bullet-}$  concentration. According to the ESR results, quenching experiments, contribution calculation of ROSs and quantification analysis of  $\text{SO}_4^{\bullet-}$ , the importance of  $\text{SO}_4^{\bullet-}$  along with the full utilization of PMS have been verified.



### 3.3.6. Possible mechanism

The surface element information of fresh and used S-BUC-21(Fe) were explored by X-ray photoelectron spectroscopy (XPS), as shown in Fig. 6a and b. In the Fe 2p spectrum, the binding energies at ca. 710.3 eV and 723.7 eV ( $\Delta = 13.4$  eV, closing to the reference [19]) were ascribed to Fe 2p<sub>3/2</sub> and Fe 2p<sub>1/2</sub>, respectively [57,69]. The corresponding satellite fitting peaks were observed at 715.4 eV and 729.8 eV. In brief, all the above four fitting peaks could be assigned to  $\text{Fe}^{3+}$ . The fitting peaks at 710.0 eV and 723.4 eV are assigned to  $\text{Fe}^{2+}$ . It could be found that the ratio of  $\text{Fe}^{2+}/\text{Fe}^{3+}$  increased from 0.78 of the fresh S-BUC-21(Fe) to 0.90 after oxidation reaction. Generally, the  $\text{Fe}^{2+}/\text{Fe}^{3+}$  ratio would decrease in Fe-based catalyst/PMS system in dark [50]. However, under UV light conditions, besides  $\text{Fe}^{2+}$ , the photo-generated electrons could also activate PMS to generate ROSs [19].  $\text{Fe}^{3+}$  could be reduced to  $\text{Fe}^{2+}$  by photo-generated electrons as well, leading to the increasing  $\text{Fe}^{2+}$  content. Another reason is that PMS could directly reduce  $\text{Fe}^{3+}$  to  $\text{Fe}^{2+}$  [70]. In this system, PMS, as electron donor, could react with S-BUC-21(Fe) and transfer  $e^-$  to reduce  $\text{Fe}^{3+}$  to  $\text{Fe}^{2+}$ . This result coincided with recent report [71], in which the  $\text{Co}^{2+}/\text{Co}^{3+}$  ratio increased from 0.32 to 0.76 after PMS activation. While, PMS is oxidized to generate  $\text{SO}_5^{\bullet-}$  and further produce  $^1\text{O}_2$ , which was consistent with the capturing experiment results. In conclusion, both PMS and UV light assisted the catalytic activity of S-BUC-21(Fe) for ATZ decomposition significantly.

Based on the above analyses and illustration, the possible mechanism of the high efficiency degradation of ATZ over S-BUC-21(Fe) on PMS activation was proposed. As shown in Fig. 6c, (i) the  $e^-$  and  $h^+$  were excited to accumulate on the HOMO and LUMO of S-BUC-21(Fe) under UV light irradiation, respectively. The  $e^-$  could not only decompose PMS to yield different ROSs, but also reduce  $\text{Fe}^{3+}$  to  $\text{Fe}^{2+}$  ( $\text{Fe}^{3+}/\text{Fe}^{2+}$ ,  $E^0 = 0.77$  V vs NHE [72]) (Eq. S7 and S8). (ii) The circling between  $\text{Fe}^{2+}$  and  $\text{Fe}^{3+}$  would promote the PMS activation to produce  $\text{SO}_4^{\bullet-}$ ,  $\bullet\text{OH}$  and  $\text{SO}_5^{\bullet-}$  (Eq. S9-S11). The  $\text{SO}_4^{\bullet-}$  and  $\bullet\text{OH}$  could efficiently degrade ATZ. Besides, S-BUC-21(Fe) could activate PMS directly to generate  $\text{SO}_5^{\bullet-}$ , which further yield  $^1\text{O}_2$  through Eq. S12. These ROSs ( $\text{SO}_4^{\bullet-}$ ,  $\bullet\text{OH}$ ,  $\bullet\text{O}_2^-$  and  $^1\text{O}_2$ ) would oxidize ATZ to form intermediates in the radical/non-radical ways.

### 3.4. Reusability, stability and universality of S-BUC-21(Fe)

As shown in Fig. 6d, 100.0 % ATZ was degraded over five cycles, indicating excellent reusability of S-BUC-21(Fe). Additionally, as shown in Fig. 6e, the XRD patterns of used S-BUC-21(Fe) were fitted well with those of the fresh one and the simulated one. In addition, as shown in

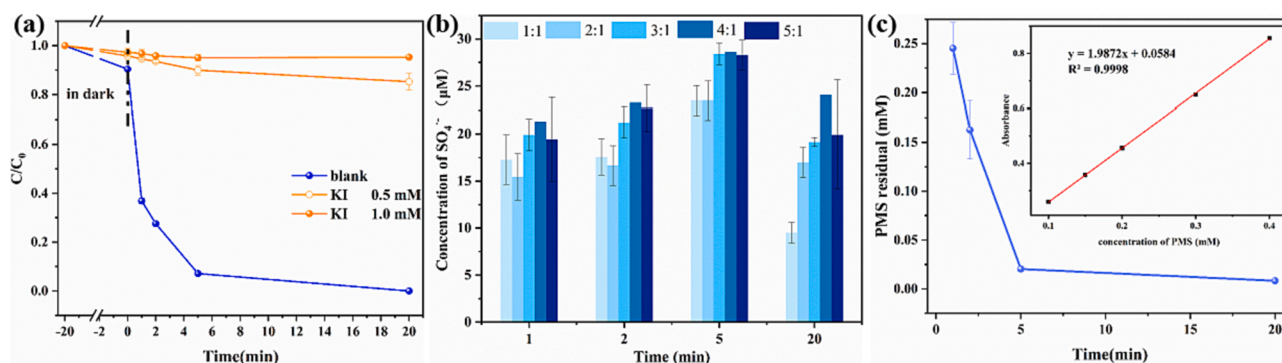
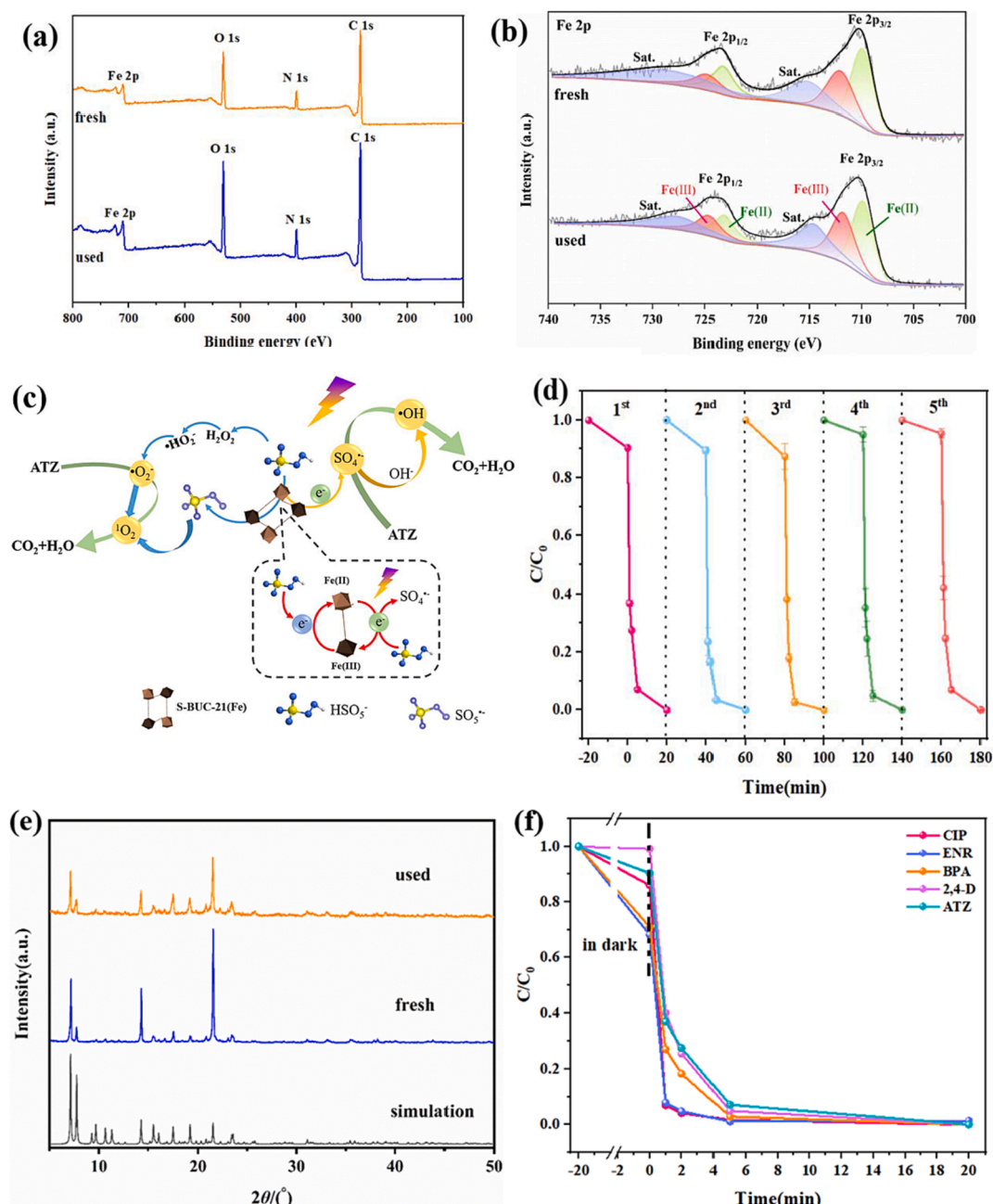


Fig. 5. (a) Surface-bound radicals capturing; (b) The concentration of  $\text{SO}_4^{\bullet-}$  in UV/S-BUC-21(Fe)/PMS system; (c) PMS Residual.



**Fig. 6.** (a) Survey and (b) Fe 2p XPS spectra of fresh and used S-BUC-21(Fe) in photocatalytic degradation of ATZ; (c) The possible mechanism of ATZ degradation in S-BUC-21(Fe)/UV/PMS system; (d) The reusability of S-BUC-21(Fe) in five runs; (e) PXRD patterns of fresh and used S-BUC-21(Fe); (f) The degradation efficiencies of CIP, ENR, BPA and 2,4-D. Reaction conditions: S-BUC-21(Fe) = 0.1 g/L, CIP, ENR, BPA, 2,4-D = 10.0 mg/L, volume = 50.0 mL, pH = 5.56, PMS = 0.4 mM.

**Table 2**

Comparison of different counterpart Fe-based catalysts for PMS activation for ATZ degradation.

catalyst	ATZ concentration (mg/L)	Radiation source	Catalyst dosage (g/L)	PMS dosage (mM)	Removal degree (%)	Time (min)	References
$\text{Fe}^{3+}/\text{Bi}_2\text{MoO}_6$	2.5	300 W Xe lamp	1.0	0.8	> 99	20	[73]
$\text{CuO-Fe}_2\text{O}_3/5\% \text{ MXene}$	10	dark	0.1	0.37	nearly 100	60	[74]
$\text{MIL-53(Fe/Co)/CeO}_2$	10	80 W visible light	0.01	0.4	99.9	60	[49]
$\text{FeCo}_2\text{O}_4/\text{rectorite}$	10	dark	0.3	0.5 mM	90.44	20	[75]
$\text{FeSx@MoS}_2\text{-x}$	10	dark	0.2	0.15 mM	100	1	[76]
$\text{TiO}_2/\text{LaFeO}_3$	2.5	200 W LED vis	0.4	0.2 mM	100	90	[77]
PCT3	10	300 W Xe lamp	0.4	0.33	75	60	[78]
$\text{CoFe}_2\text{O}_4$	10	dark	0.4	0.8	99	30	[79]
$\text{PS-Fe}_2\text{O}_3\cdot 2$	1.0784	dark	0.4	0.6	96	40	[80]
S-BUC-21(Fe)	10	10 W LED UV	0.1	0.4	100	20	This work



Fig. S4, the morphology of used S-BUC-21(Fe) wasn't changed obviously, implying that the S-BUC-21(Fe) possesses good structural stability. Therefore, the universality experiments toward different selected organic pollutants were carried out under the optimum conditions. It was found that 100.0 % degradation toward ciprofloxacin (CIP), enrofloxacin (ENR), bisphenol A (BPA) and 2,4-dichlorophenoxyacetic acid (2,4-D) with initial concentration of 10.0 mg/L were achieved within about 5.0 min on the individual pollutant system (Fig. 6f). The S-BUC-21(Fe) not only exhibited good reusability, but also possessed universality to accomplish other organic pollutants degradation. Additionally, S-BUC-21(Fe) demonstrated superior catalytic ATZ degradation performance to its counterpart Fe-based catalysts reported (Table 2).

#### 4. Conclusion

The 2D micron-sized S-BUC-21(Fe) sheet was firstly used as catalyst for PMS activation, which exhibited excellent performance for ATZ degradation in a wide range of pH from 3.5 to 9.5. ATZ was completely degraded in UV/S-BUC-21(Fe)/PMS system within 20.0 min. It was found that the  $\text{SO}_4^{\cdot-}$ ,  $\bullet\text{OH}$ ,  $\bullet\text{O}_2^-$  and  $^1\text{O}_2$  generated in the UV/S-BUC-21(Fe)/PMS system contributed to ATZ degradation. The  $\text{SO}_4^{\cdot-}$  and  $\bullet\text{OH}$  were yielded via the direct electron transfer activation over S-BUC-21(Fe) and PMS under UV irradiation. The  $\bullet\text{O}_2^-$  and  $^1\text{O}_2$  were generated from indirect transfer activation over S-BUC-21(Fe) and PMS. This work is expected to provide helpful information in identifying the formation and contributions of different reactive oxygen species for decontamination via PMS activation over Fe-based MOFs as catalysts.

#### CRediT authorship contribution statement

**Zi-Chen Zhang:** Data curation, Investigation, Visualization, Writing – original draft. **Fu-Xue Wang:** Data curation, Investigation. **Fei Wang:** Data curation. **Chong-Chen Wang:** Conceptualization, Funding acquisition, Supervision, Project administration, Writing – review & editing. **Peng Wang:** Resources.

#### Declaration of Competing Interest

The authors declare that they have no known competing financial interests or personal relationships that could have appeared to influence the work reported in this paper.

#### Data availability

Data will be made available on request.

#### Acknowledgements

This work was supported by National Natural Science Foundation of China (51878023), Beijing Talent Project (2020A27), the Pyramid Talent Training Project of Beijing University of Civil Engineering and Architecture (JDLJ20220802), and BUCEA Post Graduate Innovation Project (2021).

#### Appendix A. Supplementary material

Supplementary data to this article can be found online at <https://doi.org/10.1016/j.seppur.2022.122864>.

#### References

- [1] M. Graymore, F. Stagnitti, G. Allinson, Impacts of atrazine in aquatic ecosystems, *Environ. Int.* 26 (2001) 483–495.
- [2] B. Balci, N. Oturan, R. Cherrier, M.A. Oturan, Degradation of atrazine in aqueous medium by electrocatalytically generated hydroxyl radicals. A kinetic and mechanistic study, *Water Res.* 43 (2009) 1924–1934.
- [3] H. Zhou, Z. Xie, Y. Liu, B. Lai, W.-J. Ong, S. Wang, X. Duan, Recent advances in molybdenum disulfide-based advanced oxidation processes, *Environ. Funct. Mater.* 1 (2022) 1–9.
- [4] X.-H. Yi, T.-Y. Wang, H.-Y. Chu, Y. Gao, C.-C. Wang, Y.-J. Li, L. Chen, P. Wang, H. Fu, C. Zhao, W. Liu, Effective elimination of tetracycline antibiotics via photoactivated SR-AOP over vivianite: a new application approach of phosphorus recovery product from WWTP, *Chem. Eng. J.* 449 (2022), 137784.
- [5] Y. Zhou, J. Jiang, Y. Gao, J. Ma, S.-Y. Pang, J. Li, X.-T. Lu, L.-P. Yuan, Activation of peroxymonosulfate by benzoquinone: a novel nonradical oxidation process, *Environ. Sci. Technol.* 49 (2015) 12941–12950.
- [6] S. Wang, Y. Liu, J. Wang, Peroxymonosulfate activation by Fe–Co–O-codoped graphite carbon nitride for degradation of sulfamethoxazole, *Environ. Sci. Technol.* 54 (2020) 10361–10369.
- [7] G. Chen, Y. Yu, L. Liang, X. Duan, R. Li, X. Lu, B. Yan, N. Li, S. Wang, Remediation of antibiotic wastewater by coupled photocatalytic and persulfate oxidation system: a critical review, *J. Hazard. Mater.* 408 (2021), 124461.
- [8] H. Zhang, Q. Ji, L. Lai, G. Yao, B. Lai, Degradation of p-nitrophenol (PNP) in aqueous solution by mFe/Cu-air-PS system, *Chin. Chem. Lett.* 30 (2019) 1129–1132.
- [9] B.A. Johnson, A.M. Beiler, B.D. McCarthy, S. Ott, Transport phenomena: challenges and opportunities for molecular catalysis in metal-organic frameworks, *J. Am. Chem. Soc.* 142 (2020) 11941–11956.
- [10] C.-C. Wang, X. Ren, P. Wang, C. Chang, The state of the art review on photocatalytic Cr(VI) reduction over MOFs-based photocatalysts: from batch experiment to continuous operation, *Chemosphere* 303 (2022), 134949.
- [11] C.-Y. Wang, L. Ma, C.-C. Wang, P. Wang, L. Gutierrez, W. Zheng, Light-response adsorption and desorption behaviors of metal-organic frameworks, *Environ. Funct. Mater.* 1 (2022) 49–66.
- [12] C.-C. Wang, J.-R. Li, X.-L. Lv, Y.-Q. Zhang, G. Guo, Photocatalytic organic pollutants degradation in metal-organic frameworks, *Energy Environ. Sci.* 7 (2014) 2831–2867.
- [13] F.-X. Wang, C.-C. Wang, Fabrication approaches and organic pollutants degradation performances via advanced oxidation processes of MIL-88A(Fe) and its composites, *Res. Environ. Sci.* 34 (2021) 2924–2934.
- [14] Y.-H. Li, P. Wang, C.-C. Wang, L. Y.B., State-of-the-art review of defective metal-organic frameworks for pollutant removal from water, *Chin. J. Inorg. Chem.* 38 (2022).
- [15] Q. Zhao, C.-C. Wang, P. Wang, Effective norfloxacin elimination via photo-Fenton process over the MIL-101(Fe)-NH<sub>2</sub> immobilized on  $\alpha\text{-Al}_2\text{O}_3$  sheet, *Chin. Chem. Lett.* 33 (2022) 4828–4833.
- [16] X. Liao, F. Wang, F. Wang, Y. Cai, Y. Yao, B.-T. Teng, Q. Hao, L. Shuxiang, Synthesis of (100) surface oriented MIL-88A-Fe with rod-like structure and its enhanced fenton-like performance for phenol removal, *Appl. Catal., B* 259 (2019), 118064.
- [17] J.-S. Wang, X.-H. Yi, X. Xu, H. Ji, A.M. Alanazi, C.-C. Wang, C. Zhao, Y.V. Kaneti, P. Wang, W. Liu, Y. Yamauchi, Eliminating tetracycline antibiotics matrix via photoactivated sulfate radical-based advanced oxidation process over the immobilized MIL-88A: Batch and continuous experiments, *Chem. Eng. J.* 431 (2022), 133213.
- [18] Y. Ren, T. Li, W. Zhang, S. Wang, M. Shi, C. Shan, W. Zhang, X. Guan, L. Lv, M. Hua, B. Pan, MIL-PVDF blend ultrafiltration membranes with ultrahigh MOF loading for simultaneous adsorption and catalytic oxidation of methylene blue, *J. Hazard. Mater.* 365 (2019) 312–321.
- [19] X.-H. Yi, H. Ji, C.-C. Wang, Y. Li, Y.-H. Li, C. Zhao, A. Wang, H. Fu, P. Wang, X. Zhao, W. Liu, Photocatalysis-activated SR-AOP over PDINH/MIL-88A(Fe) composites for boosted chloroquine phosphate degradation: performance, mechanism, pathway and DFT calculations, *Appl. Catal., B* 293 (2021), 120229.
- [20] C. Zhao, J. Wang, X. Chen, Z. Wang, H. Ji, L. Chen, W. Liu, C.-C. Wang, Bifunctional Bi<sub>12</sub>O<sub>17</sub>/Cl<sub>2</sub>/MIL-100(Fe) composites toward photocatalytic Cr(VI) sequestration and activation of persulfate for bisphenol A degradation, *Sci. Total Environ.* 752 (2021), 141901.
- [21] H. Xia, J. Zhang, Z. Yang, S. Guo, S. Guo, Q. Xu, 2D MOF nanoflake-assembled spherical microstructures for enhanced supercapacitor and electrocatalysis performances, *Nano-Micro Lett.* 9 (2017) 43.
- [22] F.-X. Wang, C.-C. Wang, X. Du, Y. Li, F. Wang, P. Wang, Efficient removal of emerging organic contaminants via photo-Fenton process over micron-sized Fe-MOF sheet, *Chem. Eng. J.* 429 (2022), 132495.
- [23] W.-D. Oh, Z. Dong, G. Ronn, T.-T. Lim, Surface-active bismuth ferrite as superior peroxymonosulfate activator for aqueous sulfamethoxazole removal: performance, mechanism and quantification of sulfate radical, *J. Hazard. Mater.* 325 (2017) 71–81.
- [24] L. Ye, J. Liu, Z. Jiang, T. Peng, L. Zan, Facets coupling of BiOBr-g-C<sub>3</sub>N<sub>4</sub> composite photocatalyst for enhanced visible-light-driven photocatalytic activity, *Appl. Catal., B* (2013).
- [25] J. Jiang, X. Wang, Y. Liu, Y. Ma, T. Li, Y. Lin, T. Xie, S. Dong, Photo-Fenton degradation of emerging pollutants over Fe-POM nanoparticle/porous and ultrathin g-C<sub>3</sub>N<sub>4</sub> nanosheet with rich nitrogen defect: degradation mechanism, pathways, and products toxicity assessment, *Appl. Catal., B* 278 (2020), 119349.
- [26] W.-D. Oh, S.-K. Lua, Z. Dong, T.-T. Lim, High surface area DPA-hematite for efficient detoxification of bisphenol A via peroxymonosulfate activation, *J. Mater. Chem. A* 2 (2014) 15836–15845.
- [27] H. Jia, W. He, B. Zhang, L. Yao, X. Yang, Z. Zheng, Facile synthesis of bismuth oxyhalide nanosheet films with distinct conduction type and photo-induced charge carrier behavior, *Appl. Surf. Sci.* 441 (2018) 832–840.

- [28] L. Shen, R. Liang, M. Luo, F. Jing, L. Wu, Electronic effects of ligand substitution on metal-organic framework photocatalysts: the case study of UiO-66, *Phys. Chem. Chem. Phys.* 17 (2015) 117–121.
- [29] T. Wang, C. Zhao, L. Meng, Y. Li, H. Chu, F. Wang, Y. Tao, W. Liu, C.-C. Wang, In-situ-construction of BiOI/UiO-66 heterostructure via nanoplate-on-octahedron: a novel p-n heterojunction photocatalyst for efficient sulfadiazine elimination, *Chem. Eng. J.* 451 (2023), 138624.
- [30] M. Shirmardi, N. Alavi, E.C. Lima, A. Takdastan, A.H. Mahvi, A.A. Babaei, Removal of atrazine as an organic micro-pollutant from aqueous solutions: a comparative study, *Process Saf. Environ. Prot.* 103 (2016) 23–35.
- [31] M.L.B. Almeida, E. Ayres, F.C.C. Moura, R.L. Oréfice, Polyurethane foams containing residues of petroleum industry catalysts as recoverable pH-sensitive sorbents for aqueous pesticides, *J. Hazard. Mater.* 346 (2018) 285–295.
- [32] L. Yang, J. He, Y. Liu, J. Wang, L. Jiang, G. Wang, Characteristics of change in water quality along reclaimed water intake area of the Chaobai River in Beijing, *China, J. Environ. Sci.* 50 (2016) 93–102.
- [33] X.-W. Zhang, F. Wang, C.-C. Wang, P. Wang, H. Fu, C. Zhao, Photocatalysis activation of peroxodisulfate over the supported Fe<sub>3</sub>O<sub>4</sub> catalyst derived from MIL-88A(Fe) for efficient tetracycline hydrochloride degradation, *Chem. Eng. J.* 426 (2021), 131927.
- [34] A.A. Isse, C.Y. Lin, M.L. Coote, A. Gennaro, Estimation of standard reduction potentials of halogen atoms and alkyl halides, *J. Phys. Chem. B* 115 (2011) 678–684.
- [35] B.G. Ershov, M. Kelm, A.V. Gordeev, E. Janata, A pulse radiolysis study of the oxidation of Br<sup>-</sup> by Cl<sub>2</sub><sup>-</sup> in aqueous solution: formation and properties of ClBr<sup>-</sup>, *Phys. Chem. Chem. Phys.* 4 (2002) 1872–1875.
- [36] W. Qin, G. Fang, Y. Wang, T. Wu, C. Zhu, D. Zhou, Efficient transformation of DDT by peroxymonosulfate activated with cobalt in aqueous systems: Kinetics, products, and reactive species identification, *Chemosphere* 148 (2016) 68–76.
- [37] J.G. Nathanael, J.M. White, A. Richter, M.R. Nuske, U. Wille, Oxidative damage of proline residues by nitrate radicals (NO<sub>3</sub><sup>•</sup>): a kinetic and product study, *Org. Biomol. Chem.* 18 (2020) 6949–6957.
- [38] Y.R. Wang, W. Chu, Photo-assisted degradation of 2,4,5-trichlorophenoxyacetic acid by Fe(II)-catalyzed activation of Oxone process: the role of UV irradiation, reaction mechanism and mineralization, *Appl. Catal. B* 123–124 (2012) 151–161.
- [39] J. Li, Y. Wan, Y. Li, G. Yao, B. Lai, Surface Fe(III)/Fe(II) cycle promoted the degradation of atrazine by peroxymonosulfate activation in the presence of hydroxylamine, *Appl. Catal. B* 256 (2019), 117782.
- [40] J.-C.-E. Yang, B. Yuan, H.-J. Cui, S. Wang, M.-L. Fu, Modulating oxone-MnOx/silica catalytic systems towards ibuprofen degradation: insights into system effects, reaction kinetics and mechanisms, *Appl. Catal. B* 205 (2017) 327–339.
- [41] S. Su, C. Cao, Y. Zhao, D.D. Dionysiou, Efficient transformation and elimination of roxarsone and its metabolites by a new  $\alpha$ -FeOOH@GCA activating persulfate system under UV irradiation with subsequent As(V) recovery, *Appl. Catal., B* 245 (2019) 207–219.
- [42] N.S. Hassan, A.A. Jalil, C.N.C. Hitam, M.H. Sawal, M.N.S. Rahim, I. Hussain, N.W. C. Jusoh, R. Saravanan, D. Prasetyoko, Enhanced photooxidative desulphurization of dibenzothiophene over fibrous silica tantalum: influence of metal-disturbance electronic band structure, *Int. J. Hydrogen Energy* (2022).
- [43] W. Ren, L. Xiong, X. Yuan, Z. Yu, H. Zhang, X. Duan, S. Wang, Activation of peroxodisulfate on carbon nanotubes: electron-transfer mechanism, *Environ. Sci. Technol.* 53 (2019) 14595–14603.
- [44] F. Wang, M. Xiao, X. Ma, S. Wu, M. Ge, X. Yu, Insights into the transformations of Mn species for peroxymonosulfate activation by tuning the Mn<sub>3</sub>O<sub>4</sub> shapes, *Chem. Eng. J.* 404 (2021), 127097.
- [45] R. Li, X. Lu, B. Yan, N. Li, G. Chen, Z. Cheng, L.a. Hou, S. Wang, X. Duan, Sludge-derived biochar toward sustainable peroxymonosulfate activation: regulation of active sites and synergistic production of reaction oxygen species, *Chem. Eng. J.* 440 (2022), 135897.
- [46] A. Du, H. Fu, P. Wang, C. Zhao, C.-C. Wang, Enhanced catalytic peroxymonosulfate activation for sulfonamide antibiotics degradation over the supported CoSx-CuSx derived from ZIF-L(Co) immobilized on copper foam, *J. Hazard. Mater.* 426 (2022), 128134.
- [47] A. Jawad, K. Zhan, H. Wang, A. Shahzad, Z. Zeng, J. Wang, X. Zhou, H. Ullah, Z. Chen, Z. Chen, Tuning of persulfate activation from a free radical to a nonradical pathway through the incorporation of non-redox magnesium oxide, *Environ. Sci. Technol.* 54 (2020) 2476–2488.
- [48] C. Guan, J. Jiang, Y. Shen, S. Pang, C. Luo, X. Zhao, Carbon materials inhibit formation of nitrated aromatic products in treatment of phenolic compounds by thermal activation of peroxodisulfate in the presence of nitrite, *Environ. Sci. Technol.* 53 (2019) 9054–9062.
- [49] D. Roy, S. Neogi, S. De, Visible light assisted activation of peroxymonosulfate by bimetallic MOF based heterojunction MIL-53(Fe/Co)/CeO<sub>2</sub> for atrazine degradation: pivotal roles of dual redox cycle for reactive species generation, *Chem. Eng. J.* 430 (2022), 133069.
- [50] S. Chen, J. Deng, C. Ye, C. Xu, L. Huai, X. Ling, J. Li, X. Li, Degradation of p-arsanilic acid by pre-magnetized Fe<sup>0</sup>/persulfate system: kinetics, mechanism, degradation pathways and DBPs formation during subsequent chlorination, *Chem. Eng. J.* 410 (2021), 128435.
- [51] B. Liu, Y. Wang, X. Hao, J. Wang, Z. Yang, Q. Yang, Green synthesis of stable structure spindle FeCo-LDH through Fe-MOF template for efficient degradation of 2,4-D, *J. Water Process Eng.* 46 (2022), 102602.
- [52] G.P. Anipsitakis, D.D. Dionysiou, Radical generation by the interaction of transition metals with common oxidants, *Environ. Sci. Technol.* 38 (2004) 3705–3712.
- [53] Q. Zhou, L. Chen, L. Yan, T. Cheng, X. Wang, Y. Zhang, Singlet oxygen-dominated transformation of oxytetracycline by peroxymonosulfate with CoAl-LDH modified hierarchical porous ceramics: toxicity assessment, *Chem. Eng. J.* 436 (2022), 135199.
- [54] J. Cao, L. Lai, B. Lai, G. Yao, X. Chen, L. Song, Degradation of tetracycline by peroxymonosulfate activated with zero-valent iron: performance, intermediates, toxicity and mechanism, *Chem. Eng. J.* 364 (2019) 45–56.
- [55] L.-S. Zhang, X.-H. Jiang, Z.-A. Zhong, L. Tian, Q. Sun, Y.-T. Cui, X. Lu, J.-P. Zou, S.-L. Luo, Carbon nitride supported high-loading Fe single-atom catalyst for activation of peroxymonosulfate to generate <sup>1</sup>O<sub>2</sub> with 100 % selectivity, *Angew. Chem., Int. Ed.* 60 (2021) 21751–21755.
- [56] Y. Liu, H. Guo, Y. Zhang, W. Tang, X. Cheng, W. Li, Heterogeneous activation of peroxymonosulfate by silicite Bi<sub>25</sub>FeO<sub>40</sub>: singlet oxygen generation and degradation for aquatic levofloxacin, *Chem. Eng. J.* 343 (2018) 128–137.
- [57] X. Hu, H. Ji, L. Wu, Singlet oxygen photogeneration and 2,4,6-TCP photodegradation at Pt/TiO<sub>2</sub> under visible light illumination, *RSC Adv.* 2 (2012) 12378–12383.
- [58] Q. Zhang, D. He, X. Li, W. Feng, C. Lyu, Y. Zhang, Mechanism and performance of singlet oxygen dominated peroxymonosulfate activation on CoOOH nanoparticles for 2,4-dichlorophenol degradation in water, *J. Hazard. Mater.* 384 (2020), 121350.
- [59] Z. Xu, Y. Wu, Q. Ji, T. Li, C. Xu, C. Qi, H. He, S. Yang, S. Li, S. Yan, C. Sun, L. Zhang, Z. Zou, Understanding spatial effects of tetrahedral and octahedral cobalt cations on peroxymonosulfate activation for efficient pollution degradation, *Appl. Catal., B* 291 (2021), 120072.
- [60] Z. Li, Y. Sun, Y. Yang, Y. Han, T. Wang, J. Chen, D.C.W. Tsang, Comparing biochar and bentonite-supported Fe-based catalysts for selective degradation of antibiotics: mechanisms and pathway, *Environ. Res.* 183 (2020), 109156.
- [61] P. Li, J. Li, X. Feng, J. Li, Y. Hao, J. Zhang, H. Wang, A. Yin, J. Zhou, X. Ma, B. Wang, Metal-organic frameworks with photocatalytic bactericidal activity for integrated air cleaning, *Nat. Commun.* 10 (2019) 2177.
- [62] Y. Wu, Y. Xing, X. Zhao, Z. Zhou, G. Jing, Mechanistic insights into rapid sulfite activation with cobalt sulfide towards iohexol abatement: Contribution of sulfur conversion, *Chem. Eng. J.* 429 (2022), 132404.
- [63] Y. Chen, M. Li, Y. Tong, Z. Liu, L. Fang, Y. Wu, Z. Fang, F. Wu, L.-Z. Huang, Radical generation via sulfite activation on NiFe<sub>2</sub>O<sub>4</sub> surface for estril removal: performance and mechanistic studies, *Chem. Eng. J.* 368 (2019) 495–503.
- [64] D.T. Oyekunle, B. Wu, F. Luo, J. Ali, Z. Chen, Synergistic effects of Co and N doped on graphitic carbon as an in situ surface-bound radical generation for the rapid degradation of emerging contaminants, *Chem. Eng. J.* 421 (2021), 129818.
- [65] T. Zhang, C. Li, J. Ma, H. Tian, Z. Qiang, Surface hydroxyl groups of synthetic  $\alpha$ -FeOOH in promoting OH generation from aqueous ozone: property and activity relationship, *Appl. Catal., B* 82 (2008) 131–137.
- [66] S.-S. Lin, M.D. Gurol, Catalytic decomposition of hydrogen peroxide on iron oxide: kinetics, mechanism, and implications, *Environ. Sci. Technol.* 32 (1998) 1417–1423.
- [67] Y. Feng, P.-H. Lee, D. Wu, K. Shih, Surface-bound sulfate radical-dominated degradation of 1,4-dioxane by alumina-supported palladium (Pd/Al<sub>2</sub>O<sub>3</sub>) catalyzed peroxymonosulfate, *Water Res.* 120 (2017) 12–21.
- [68] F. Wang, H. Fu, F.-X. Wang, X.-W. Zhang, P. Wang, C. Zhao, C.-C. Wang, Enhanced catalytic sulfamethoxazole degradation via peroxymonosulfate activation over amorphous CoSx@SiO<sub>2</sub> nanocages derived from ZIF-67, *J. Hazard. Mater.* 423 (2022), 126998.
- [69] Q. Chen, J. Li, L. Cheng, H. Liu, Construction of CdLa<sub>2</sub>S<sub>4</sub>/MIL-88A(Fe) heterojunctions for enhanced photocatalytic H<sub>2</sub>-evolution activity via a direct Z-scheme electron transfer, *Chem. Eng. J.* 379 (2020), 122389.
- [70] Q. Wang, J. Lu, Y. Jiang, S. Yang, Y. Yang, Z. Wang, FeCo bimetallic metal organic framework nanosheets as peroxymonosulfate activator for selective oxidation of organic pollutants, *Chem. Eng. J.* 443 (2022), 136483.
- [71] F.-X. Wang, Z.-C. Zhang, X.-H. Yi, C.-C. Wang, P. Wang, C.-Y. Wang, B. Yu, A micron-sized Co-MOF sheet to activate peroxymonosulfate for efficient organic pollutant degradation, *CrystEngComm* 24 (2022) 5557–5561.
- [72] T. Guo, K. Wang, G. Zhang, X. Wu, A novel  $\alpha$ -Fe<sub>2</sub>O<sub>3</sub>@g-C<sub>3</sub>N<sub>4</sub> catalyst: synthesis derived from Fe-based MOF and its superior photo-Fenton performance, *Appl. Surf. Sci.* 469 (2019) 331–339.
- [73] Z. Shen, H. Zhou, P. Zhou, H. Zhang, Z. Xiong, Y. Yu, G. Yao, B. Lai, Degradation of atrazine in water by Bi<sub>2</sub>MoO<sub>6</sub> and visible light activated Fe<sup>3+</sup>/peroxymonosulfate coupling system, *J. Hazard. Mater.* 425 (2022), 127781.
- [74] P. Xu, P. Wang, X. Li, R. Wei, X. Wang, C. Yang, T. Shen, T. Zheng, G. Zhang, Efficient peroxymonosulfate activation by CuO-Fe<sub>2</sub>O<sub>3</sub>/MXene composite for atrazine degradation: Performance, coexisting matter influence and mechanism, *Chem. Eng. J.* 440 (2022), 135863.
- [75] Z. Sun, X. Liu, X. Dong, X. Zhang, Y. Tan, F. Yuan, S. Zheng, C. Li, Synergistic activation of peroxymonosulfate via in situ growth FeCo<sub>2</sub>O<sub>4</sub> nanoparticles on natural rectorite: role of transition metal ions and hydroxyl groups, *Chemosphere* 263 (2021), 127965.
- [76] F. Wang, S.-S. Liu, Z. Feng, H. Fu, M. Wang, P. Wang, W. Liu, C.-C. Wang, High-efficient peroxymonosulfate activation for rapid atrazine degradation by FeSx@MoS<sub>2</sub> derived from MIL-88A(Fe), *J. Hazard. Mater.* 440 (2022), 129723.
- [77] K. Wei, A. Armutulu, Y. Wang, G. Yao, R. Xie, B. Lai, Visible-light-driven removal of atrazine by durable hollow core-shell TiO<sub>2</sub>@LaFeO<sub>3</sub> heterojunction coupling with peroxymonosulfate via enhanced electron-transfer, *Appl. Catal., B* 303 (2022), 120889.
- [78] R. Tang, D. Gong, Y. Deng, S. Xiong, J. Deng, L. Li, Z. Zhou, J. Zheng, L. Su, L. Yang,  $\pi$ - $\pi$  Stacked step-scheme PDI/g-C<sub>3</sub>N<sub>4</sub>/TiO<sub>2</sub>@Ti<sub>3</sub>C<sub>2</sub> photocatalyst with enhanced

- visible photocatalytic degradation towards atrazine via peroxymonosulfate activation, *Chem. Eng. J.* 427 (2022), 131809.
- [79] J. Li, M. Xu, G. Yao, B. Lai, Enhancement of the degradation of atrazine through  $\text{CoFe}_2\text{O}_4$  activated peroxymonosulfate (PMS) process: kinetic, degradation intermediates, and toxicity evaluation, *Chem. Eng. J.* 348 (2018) 1012–1024.
- [80] H. Zheng, J. Bao, Y. Huang, L. Xiang, B. Faheem, J. Ren, M.N. Du, D.D. D. Nadagouda, Efficient degradation of atrazine with porous sulfurized  $\text{Fe}_2\text{O}_3$  as catalyst for peroxymonosulfate activation, *Appl. Catal. B* 259 (2019), 118056.